Journal of the Optical Society of America A
OPTICS, IMAGE SCIENCE, AND VISION

Multi-wavelength unidirectional forward scattering properties of the arrow-shaped gallium phosphide nanoantenna

JINGWEI LV,[1] YANRU REN,[1] DEBAO WANG,[1] XINCHEN XU,[1] WEI LIU,[1] JIANXIN WANG,[1] CHAO LIU,[1,*] AND PAUL K CHU[2]

[1]School of Physics and Electronic Engineering, Northeast Petroleum University, Daqing 163318, China
[2]Department of Physics, Department of Materials Science and Engineering, and Department of Biomedical Engineering, City University of Hong Kong, Tat Chee Avenue, Kowloon, Hong Kong, China
*msm-liu@126.com

Received 26 May 2023; revised 8 August 2023; accepted 30 September 2023; posted 2 October 2023; published 19 October 2023

An arrow-shaped gallium phosphide nanoantenna exhibits both near-field electric field enhancement and far-field unidirectional scattering, and the interference conditions involve electric and magnetic quadrupoles as well as toroidal dipoles. By using long-wavelength approximation and exact multipole decomposition, the interference conditions required for far-field unidirectional transverse light scattering and backward near-zero scattering at multiple wavelengths are determined. The near-field properties are excellent, as exemplified by large Purcell factors of 4.5×10^9 for electric dipole source excitation, 464.68 for magnetic dipole source excitation, and 700 V/m for the field enhancement factor. The degree of enhancement of unidirectional scattering is affected by structural parameters such as the angle and thickness of the nanoantenna. The arrow-shaped nanoantenna is an efficient platform to enhance the electric field and achieve high directionality of light scattering. Moreover, the nanostructure enables flexible manipulation of light waves and materials, giving rise to superior near-field and far-field performances, which are of great importance pertaining to the practicability and application potential of optical antennas in applications such as spectroscopy, sensing, displays, and optoelectronic devices.

https://doi.org/10.1364/JOSAA.496501

1. INTRODUCTION

Nanoantennas have garnered significant interest because they can support highly localized surface plasmon resonance and control the directionality of light scattering [1]. In particular, the plasmonic nanoantenna composed of noble metals has the ability to confine light to deep-subwavelength volumes and produce a substantial gain in directivity in the visible light range because of localized surface plasmon resonance (LSPR) [2]. However, metal nanoparticles have low efficiency due to their intrinsic ohmic loss [3]. Nanostructures composed of high-refractive-index materials can manipulate light at optical frequencies and are attractive to optical communication [4], optical sensing [5,6], biophysics [7], astrophysics [8], and materials science [9].

With the development of nanoscale manufacturing, the size, shape, and materials of subwavelength-sized dielectric nanostructures, such as GaP nanoantennas [10], gallium phosphide nanodisks [11], and GaP NPs [12], can be tailored in accordance with the need and utility. Therefore, controlling light scattering at the subwavelength scale has gained increasing interest. The directionality of light scattering is determined by different electromagnetic multipole moments of the scattering medium, and interference between the electric dipole (ED) and higher-order multipoles can be utilized to engineer the radiation pattern, where the scattered light is highly directional. Unidirectional nanoantennas possess the capability of providing directionality to non-directional light emitters such as microlasers, nanolasers, plasma lasers, or even quantum dots. Recent developments in plasmonics and metamaterials have spurred the development of new nanoantennas for unidirectional light scattering, for instance, nanodisks [13], nanospheres [14], nanoblocks [15], antenna array plasma nanoantennas [16], and some complex structures like bimetallic plasmonic nanoantennas [17], plasmonic trimers [14], and large-area plasmonic nanoparticles [18].

The U-shaped split-ring resonator can also support the electric dipole, quadrupole, and magnetic dipole (MD) moments for a compact directional optical antenna [19]. Zhang *et al*. have demonstrated that a touching dielectric (T-shaped) nanoantenna can support a broad ED mode that spectrally overlaps the MD mode with high directionality [20]. According to Yu *et al*., unidirectional transverse light scattering in a V-shaped silicon nanoantenna involves the balance of the magnetic quadrupole moment [21]. Terekhov *et al*. have proposed directional light

scattering with the toroidal moment in silicon nanocylinders [22] and in silicon nanopyramids [23]. Even though highly unidirectional light scattering can be accomplished for dielectric nanoantennas by rational design, obtaining multiple unidirectional responses still remains a challenge. The near-field strength in dielectric nanoantennas can be adjusted by changing the length, width, and height, and better properties can be obtained compared to plasmonic nanoantennas. Therefore, new nanoantennas composed of all-dielectric nanoantennas are important for achieving multiple unidirectional responses and enhancing the electric field enhancement simultaneously.

Herein, an arrow-shaped gallium phosphide nanoantenna that can suppress background scattering and enhance forward directional scattering is investigated using the finite element method (FEM). GaP is suitable for low-loss nanophotonic antennas in the optical regime because its bandgap wavelength is as small as 550 nm, and the refractive index is 3.3 [10]. The multipole contributions of the scattering cross section and the directional scattering upon the plane wave illumination are studied. The directional far-field emission of the electric and magnetic dipole emitters placed close to the arrow-shaped nanoantenna is investigated. The nanoantenna exhibits unidirectional forward scattering with high efficiency not limited to one specific wavelength, and it can be adapted to multiple wavelengths. Enhanced unidirectional scattering can be accomplished by adjusting the geometric parameters of the nanoantenna. The enhanced photon and electron coupling in the nanostructure make the near-field intensity approximately 700 V/m. The Purcell factor (PF) is evaluated when a point dipole emitter is used for forward scattering. The arrow-shaped gallium phosphide nanoantenna, which combines one-way scattering enhancement and remarkable spontaneous radiation performance, has the potential to become a high-performance nanoantenna with promising applications in nano-electronics [24,25], photovoltaic devices [26], and light-emitting devices [27], as well as in biosensing [28], surface-enhanced spectroscopy [29], and quantum emission [30].

2. MULTIPOLE COMPOSITION METHOD

Different models are usually adopted to investigate the near-field and far-field characteristics of nanoantennas. The incident light can activate different electromagnetic resonance modes, and when two or more modes cooperate, the scattering characteristics of the far field are triggered in the long wavelength approximation. In order to elucidate the physical mechanism of coupling between various modes, the multipole expansions in Cartesian coordinates, including the electric dipole moment P_α (ED), the magnetic dipole moment M_α (MD), the toroidal dipole moment T_α (TD), the electric quadrupole moment $Q^e_{\alpha\beta}$ (EQ), and the magnetic quadrupole moment $Q^m_{\alpha\beta}$ (MQ) are employed to analyze the properties of the scattering cross section and their definitions are shown as follows [20,31]:

$$P_\alpha = \frac{1}{iw}\int J_\alpha \mathrm{d}^3 r, \tag{1}$$

$$M_\alpha = \frac{1}{2c}\int [r \times J]_\alpha \mathrm{d}^3 r, \tag{2}$$

$$T_\alpha = \frac{1}{10c}\int \left[(r\cdot J)_{r_\alpha} - 2r^2 J_\alpha\right] \mathrm{d}^3 r, \tag{3}$$

$$Q^e_{\alpha\beta} = -\frac{1}{iw}\int \left[r_\alpha J_\beta + J_\alpha r_\beta - \frac{2}{3}\delta_{\alpha\beta}(r\cdot J)\right] \mathrm{d}^3 r, \tag{4}$$

$$Q^m_{\alpha\beta} = \frac{1}{3c}\int \left[[r\times J]_\alpha r_\beta + r_\alpha [r\times J]_\beta\right] \mathrm{d}^3 r, \tag{5}$$

where r is the distance vector, j stands for the excited polarization current density in the antenna, and the subscripts represent the EQ and MQ component parts. The radiation power I of the various multipole moments can be calculated as follows [32]:

$$I = \frac{1}{8\pi\varepsilon_0}\left[\frac{2\omega^4}{3c^3}|P_\alpha|^2 + \frac{2\omega^4}{3c^3}|M_\alpha|^2 + \frac{4\omega^5}{3c^4}\mathrm{Im}\left(P_\alpha{}^* T_\alpha\right) + \frac{2\omega^6}{3c^5}|T_\alpha|^2 + \frac{\omega^6}{20c^5}\sum |Q^e_{\alpha\beta}|^2 + \frac{\omega^6}{20c^5}\sum |Q^m_{\alpha\beta}|^2\right]. \tag{6}$$

In addition, the total radiated power and total scattering cross section (SCS) can be mathematically represented by the following equation:

$$C_{sc\alpha} = \frac{I}{I_{\mathrm{inc}}}, \tag{7}$$

where I_{inc} is the radiation power of the incident light wave.

Figure 1(a) shows the schematic of the arrow-shaped dielectric nanoantenna with a top angle α of 15° and a height H of 420 nm. The width A and length B of the tail are 40 nm and 100 nm, respectively. The scattering properties of the arrow-shaped nanoantenna are derived by COMSOL 6.0 Multiphysics based on the FEM. A circular perfectly matched layer (PML) is established as the absorbing boundary condition in the three-dimensional modeling engaged to decrease unnecessary electromagnetic reflection [33]. In the simulation, convergence tests are carried out by optimizing the mesh size and PML thickness to produce more accurate results [34]. The structure is assumed to be freestanding in air (dielectric constant $\varepsilon = 1$) and illuminated with a normal-incident plane wave (k along the z-direction) that is linearly polarized along the x-axis. Gallium phosphide (GaP), which has low-loss characteristics in the visible region, is selected for the nanoantenna [35,36], and the refractive index of GaP is taken from Palik's handbook [37]. Oh *et al*. demonstrated the guided domino lithography (GDL) process to fabricate uniform ultra-sharp nanoantenna arrays by controlling both geometries of the photoresist patterns and the exposing doses [38]. The fabrication of arrow-shaped nanoantennas can be achieved by utilizing the mechanical collapse of nanostructures.

3. RESULTS AND DISCUSSION

In order to conduct a detailed analysis of the scattering features of the nanoantenna, the 3D far-field distributions of the GaP arrowhead antenna is presented at different forward/backward scattering (FS/BS) wave peak positions along with the corresponding wavelengths. Specifically, the radiation in the

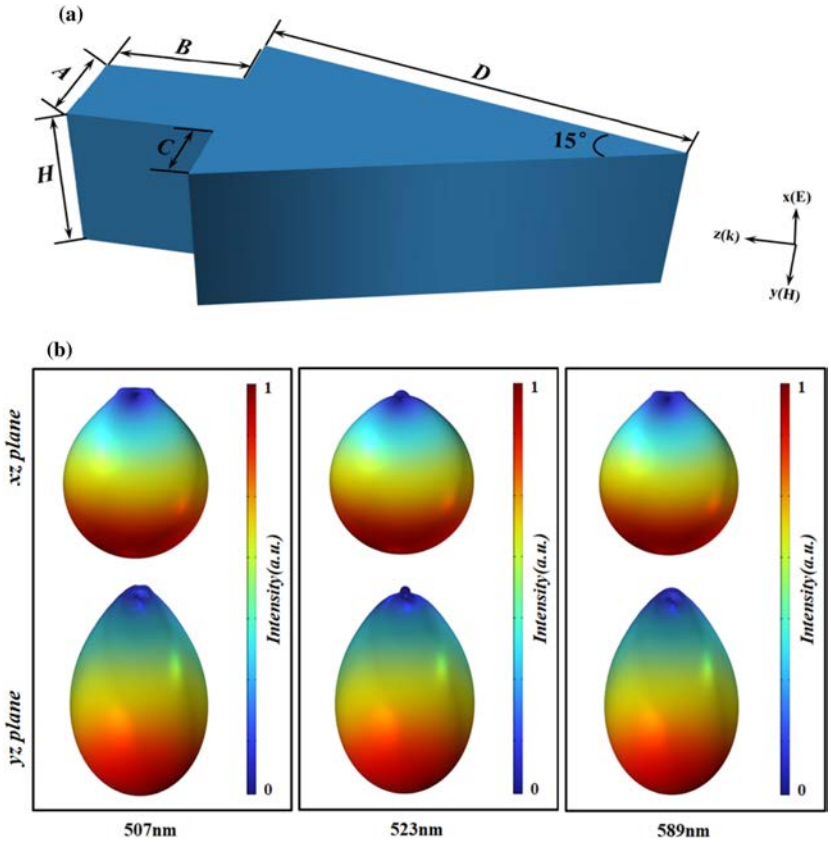

Fig. 1. (a) Schematic illustration of the arrow-shaped gallium phosphide nanoantenna for COMSOL Multiphysics simulation at $\lambda = 507$ nm, $\lambda = 523$ nm, and $\lambda = 589$ nm and (b) 3D far-field radiation patterns of the GaP arrowhead antenna.

$-z$-direction almost completely cancels out, whereas that in the $+z$-direction is enhanced. The forward scattering can be explained by the interferences between the electromagnetic fields produced by the multipoles.

In order to analyze the origin of the electromagnetic resonance mode, the multipole decomposition of the nanoantenna at wavelengths ranging from 480 to 850 nm is presented in Fig. 2, which shows four distinct resonance peaks at $\lambda = 485$ nm, $\lambda = 515$ nm, $\lambda = 532$ nm, and $\lambda = 559$ nm in the total scattering cross section. It is found to be in excellent agreement with the wavelength range of the total SCS obtained from the experimental verifications [10,12]. The peaks can be attributed to the different multipole moments which enable the interpretation of the optical properties of the arrow-shaped nanoantenna. The resonance peaks at 485 nm and 559 nm stem from the coupling effects of the TD and the MD and those at 515 nm and 532 nm arise from the coupling effects of the TD, the MD, and the MQ. In comparison with the other modes, the ED moment is relatively weak and negligible. The total scattering cross section is dominated by the TD moment, and the high-order resonant modes (including the TD) play crucial roles in the modulation of the far-field energy of high-refractive-index dielectric nanoantennas.

To investigate the far-field scattering characteristics of the nanoantenna, the forward (FS), backward (BS), and forward/backward scattering (FS/BS) cross section are calculated for the wavelength range between 470 and 650 nm [Fig. 3(a)].

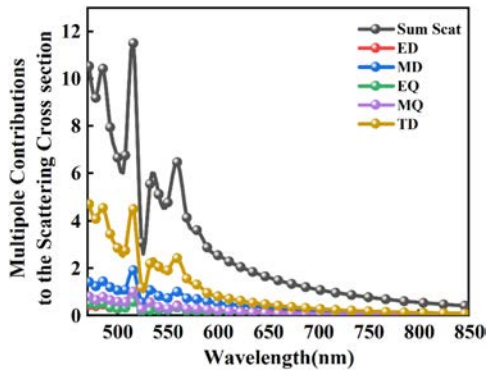

Fig. 2. Multipole contributions to the scattering cross sections.

The FS and BS cross sections can be determined by the integral of the Poynting vector in the semi-space with the z coordinate <0 and the z coordinate >0. As shown in Fig. 3(a), the energy of the BS is significantly lower than that of the FS in the spectrum. In addition, three different plasmon resonance peaks appear from the FS/BS curve with peaks at 507 nm, 523 nm, and 589 nm and corresponding intensity ratios of 13.7, 15.5, and 11.9, respectively, thus revealing good directionality.

In order to analyze the fundamentals of directional forward scattering, different phases of multipole moments are given in Fig. 3(b). At the frequency of FS/BS_{max}, the magnitudes of the scattered electric fields contributed by the TD and the MD exhibit much greater amplitudes than those from the MQ, the

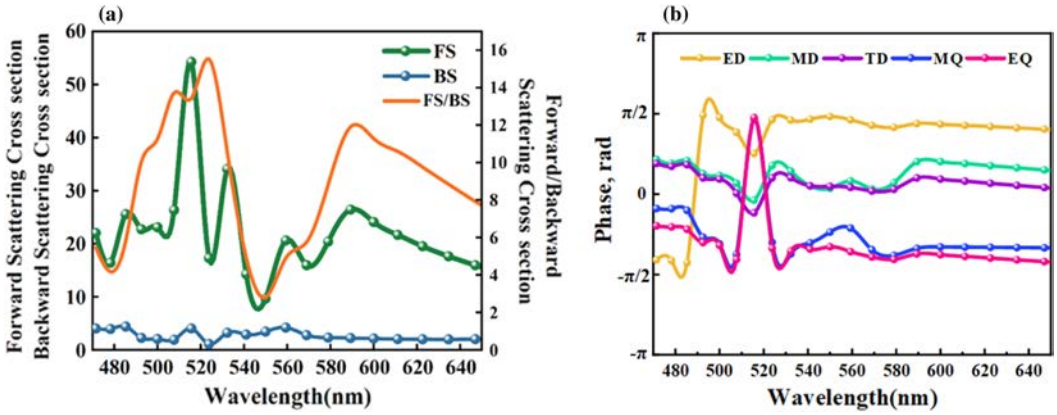

Fig. 3. (a) Forward, backward, and forward/backward scattering spectra. (b)The phase of different multipole moments, including the electric dipole (ED), the magnetic dipole (MD), the toroidal dipole (TD), the electric quadrupole (EQ), and the magnetic quadrupole (MQ).

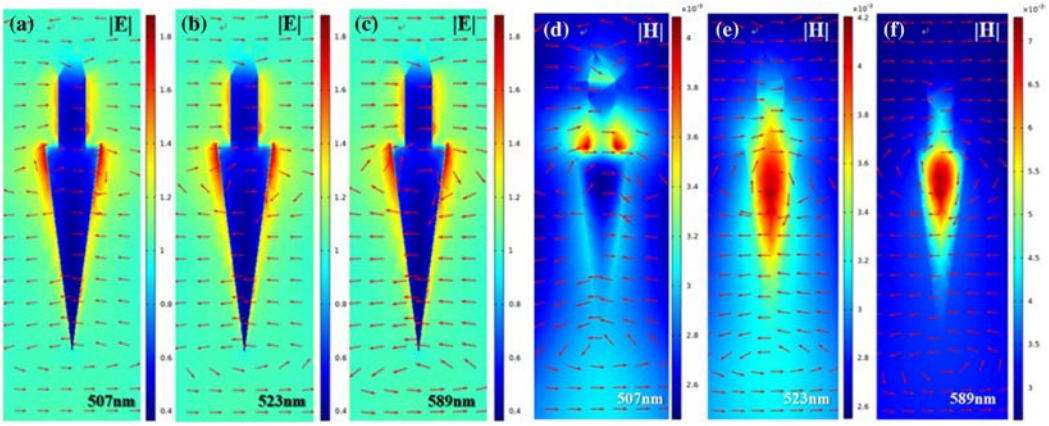

Fig. 4. Spatial profile. (a)–(c) The electric fields and (d)–(f) the magnetic fields at the wavelengths of FS/BS_{max}.

EQ, and the ED. Therefore, it is appropriate to consider the TD and the MD at three different plasmon resonance peaks. The phase differences of scattered electric fields generated by the TD and the MD are very small [39]. Hence, they will constructively interfere in the forward direction, yielding strong forward scattering at 507 nm, 523 nm, and 589 nm.

In order to gain more information, Fig. 4 shows the spatial distributions of the electric and magnetic fields at 507 nm, 523 nm, and 589 nm. The electric field distributions in Figs. 4(a)–4(c) exhibits dispersed electric fields at the tip edge, and the current distributions are shown by the red arrows. The displacement currents in the dielectrics, in contrast to the conduction current in the liberated-electron metal, is generated by oscillations of bound electrons caused by field penetration and phase-delay effects of the particles [40]. Figures 4(d)–4(f) present the magnetic field intensity distributions of the three resonance peaks in the YOZ plane. The magnetic hot spots at the different wavelengths are dissimilar. At $\lambda = 507$ nm, two comparatively small magnetic hot spots are observed from the edges of the structure. However, the magnetic hotspots are mainly distributed in the center and the intensity increases significantly at $\lambda = 523$ nm and $\lambda = 589$ nm.

To further examine the properties of unidirectional scattering of the arrow-shaped nanoantenna, Fig. 5(a) shows the angular distributions of the 2D far-field scattering intensity at the wavelength of the FS/BS maximum. Significant suppression of BS and the strong enhancement of the FS are observed at the wavelength of the FS/BS peaks, and the unidirectional forward interference produces strong forward scattering at these wavelengths. Furthermore, the polar decay of the backscattering is closely linked to the multipole decomposition of the nanoparticle scattering. The interference between multiple induction modes of the multipole and the unfolded electromagnetic field can be used to explain the directionality, and, as shown in Fig. 5(b), the 3D far-field patterns exhibit unidirectional scattering when the wavelengths are 507 nm, 523 nm, and 589 nm.

Directionality plays an important role in the application of antennas, as it shows the ratio of the power density of the antenna in the most concentrated direction to the power density of a theoretically isotropic transmitter with the same total power transmission level. A larger value indicates that the beam is more concentrated. In the study of the effects of the structural parameters B, Θ and H for unidirectional scattering and the positive backward ratio (FB) are used to characterize the spectral dependence of the three parameters. Here, the FB ratio is defined as $G_{FB} = 10\log_{10}(SF/SB)$, where SF denotes the 90° positive direction and SB represents the power amplitude radiated at 270° in the opposite direction [41].

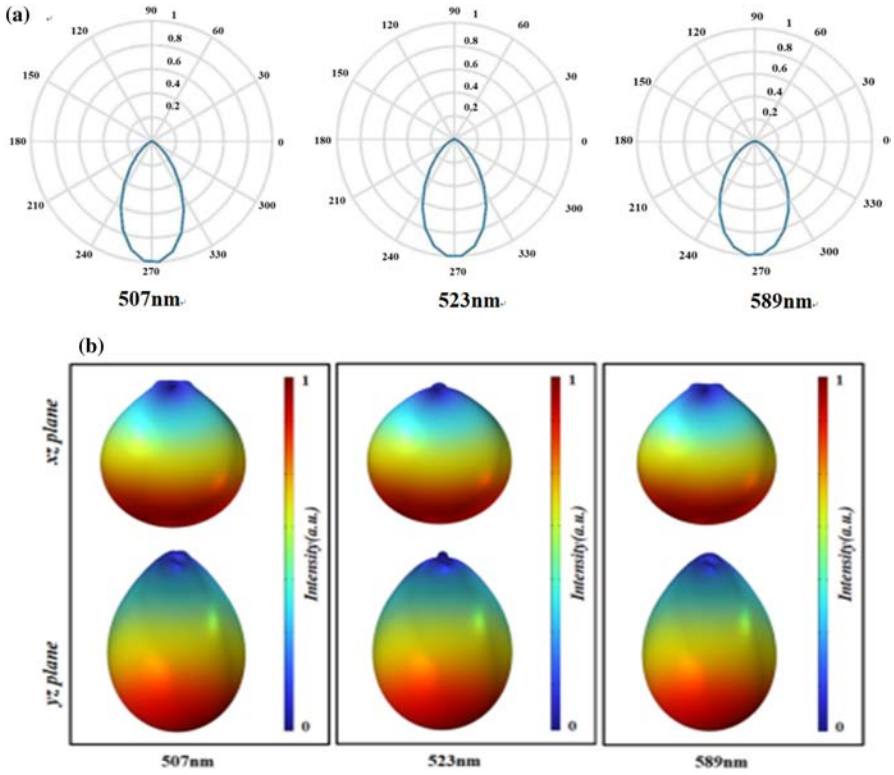

Fig. 5. (a) Scattering patterns of the arrow-shaped gallium phosphide nanoantenna (2D) and (b) 3D far-field radiation patterns of the arrow-shaped gallium phosphide nanoantenna.

Figures 6(a)–6(i) show the specific enhancement process for the three structural components B, Θ, and H. The three graphical representations, namely, the structure maps [6(a), 6(d), 6(g)], isopach maps [6(b), 9(e), 6(h)], and histograms [6(c), 6(f), 6(i)], collectively demonstrate the spectral dependence of the far-field forward-backward (FB) directionality as functions of B, Θ, and H. Figures 6(a) and 6(b) indicate that the trend of G_{FB} is consistent when B is changed from 20 to 100 nm and increases gradually with increasing B. Figure 6(c) shows that the values of G_{FB} max at resonant wavelengths of 507 nm, 532 nm, and 589 nm occur at $B = 100$ nm corresponding to 11.3 [dB], 11.9 [dB], and 10.7 [dB], respectively. Figure 6(e) presents the highest and lowest energy, specifically G_{FB}, in the representative right-hand color card, denoted by dark red and blue colors, respectively. The color turns from light to dark red when Θ is varied from 60° to 15°, explaining the maximum energy of the light field at 15°. As shown in Fig. 6(f), the maximum values of G_{FB} at the resonant peaks of 507 and 523 nm are significantly higher when the arrow angle of 15° compared to other angles, whereas G_{FB} max at 589 nm shows no obvious numerical pattern and the difference is not statistically significant. The reliance of G_{FB} on the resonance wavelength for different thicknesses (140–420 nm) is shown in Figs. 6(g)–6(i). As H becomes larger, the resonance wavelength shifts to longer wavelengths because of the phase overshot. Moreover, the intensities of the G_{FB} peaks at 507 nm, 532 nm, and 589 nm increase as H goes up from 140 to 420 nm. The enhancement of unidirectional scattering is facilitated by an increase in the thickness. In summary, the optimal structural parameters of the arrow-type nanoantenna are $B = 100$ nm, $\Theta = 15°$, and $H = 420$ nm, which can be adopted for surface-enhanced fluorescence emission (SEF). Moreover, the arrow-shaped nanoantenna with the tip cut off can still exhibit unidirectional scattering (see Figure S1 in Supplement 1).

Figure 7(a) shows the scattering cross section of the arrow-shaped nanoantenna suspended in media with the indexes ranging from $n = 1$ to $n = 1.5$. The forward/backward scattering (FS/BS) cross section is calculated shown in Fig. 7(b). There is subtle red shift or blue shift as the surrounding medium increases. In addition, the intensity of SCS increases with the increasing refractive index. As the refractive index changes from 1.0 to 1.5, broadband forward scattering can be achieved. The broadband forward scattering effect is affected by the surrounding medium [42].

To further boost the directionality of the unidirectional scattering, an array of dielectric nano-antennas along the z-axis is employed, as shown in Fig. 8 [43]. As shown in Fig. 8(a), the number of nanoparticles is added along the z-axis and the particle distance $L = 200$ nm is arranged in the same direction in a sequential manner. The operating wavelengths at the peak of the G_{FB} spectra are taken from Figs. 8(b)–8(e) for the 2D and 3D far-field investigation, corresponding to resonances at 523 nm and 589 nm, respectively. Figures 8(b) and 8(d) show that the main flap beam at 523 nm undergoes a narrowing process when the number of particles is varied from 1 to 3, indicating that the directionality is greatly enhanced by the array. The 3D far-field diagrams in Figs. 8(c) and 8(e) confirm our analysis. The 3D far-field diagram shows that the main lobe beam width decreases as

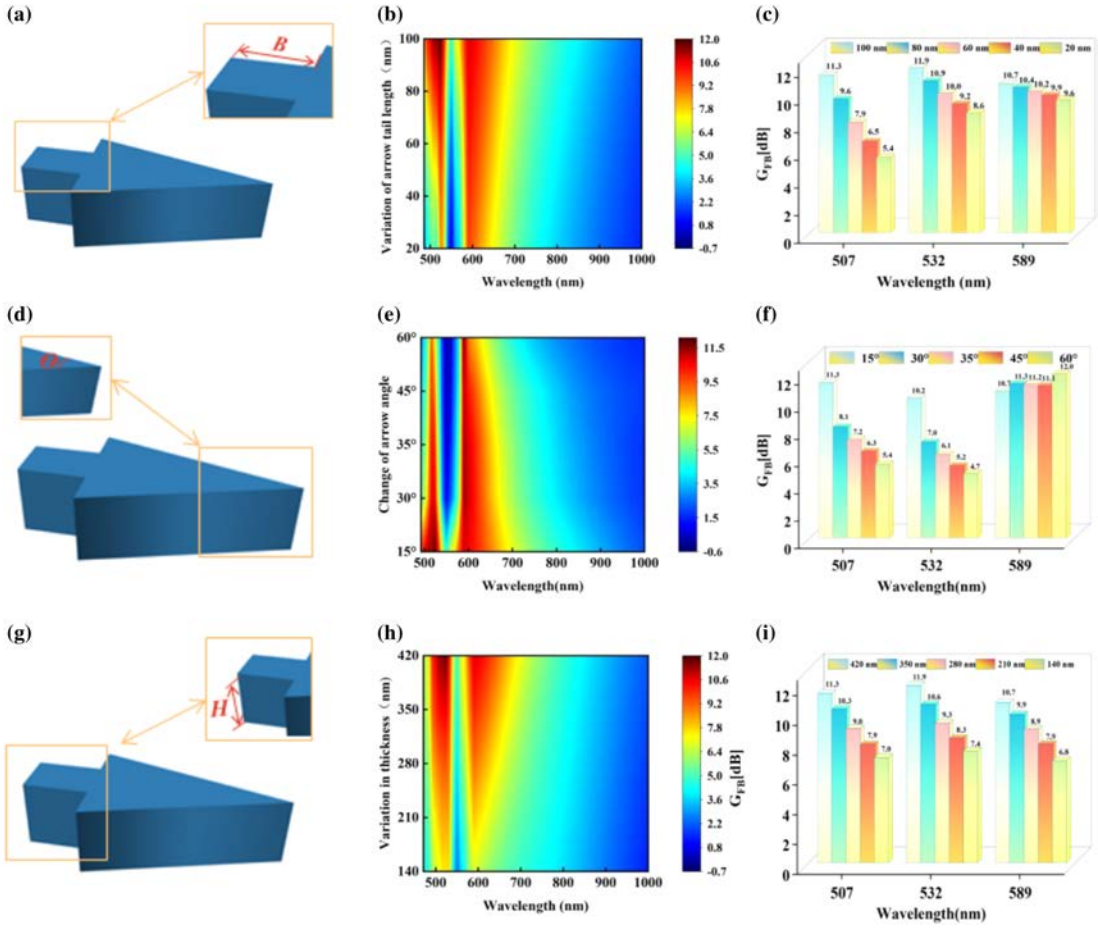

Fig. 6. (a),(d),(g) $G_{FS/BSmax}$ of the arrow-shaped nanoantenna with different structural parameters B, Θ, and H. Far-field forward-to-backward directionality $G_{FS/BSmax}$ for gap arrow-shaped nanoantenna with different (b) tail-length B, (e) angle Θ, and (h) thicknesses H. (b),(e),(h) Dependence of $G_{FS/BSmax}$ on wavelengths with B, Θ, and H. Histograms showing the maximum G_{FB} as a function of wavelength for different (c) tail lengths B, (f) angles Θ, and (i) thicknesses H.

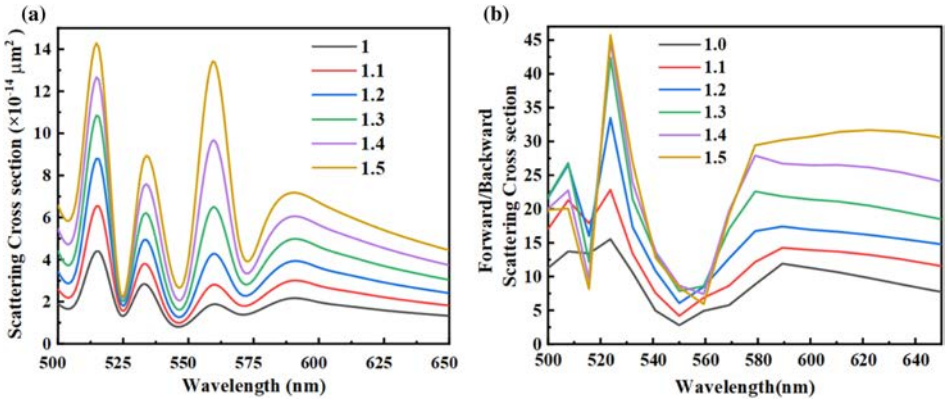

Fig. 7. (a) The scattering cross section and (b) forward/backward scattering (FS/BS) cross section for the refractive index n from 1.0 to 1.5.

the number of particles increases, and it also triggers the appearance of some tiny side scattering lobes. Further investigation reveals that the side flaps are generated by the interference effects of higher order modes.

Although the directionality is crucial to nanoantennas, the Purcell factor (PF) also makes an irreplaceable contribution, as shown below [44–46],

$$\mathrm{PF} = \frac{P}{P_0},$$

$$P_0 = \frac{\omega^4 |P_0|^2}{12\pi\varepsilon_0 c^3},$$

where P_0 is the power lost by an MD without a resonator in vacuum, and P is the power lost by an electric or magnetic dipolar emitter in the presence of the disk inside the resonator.

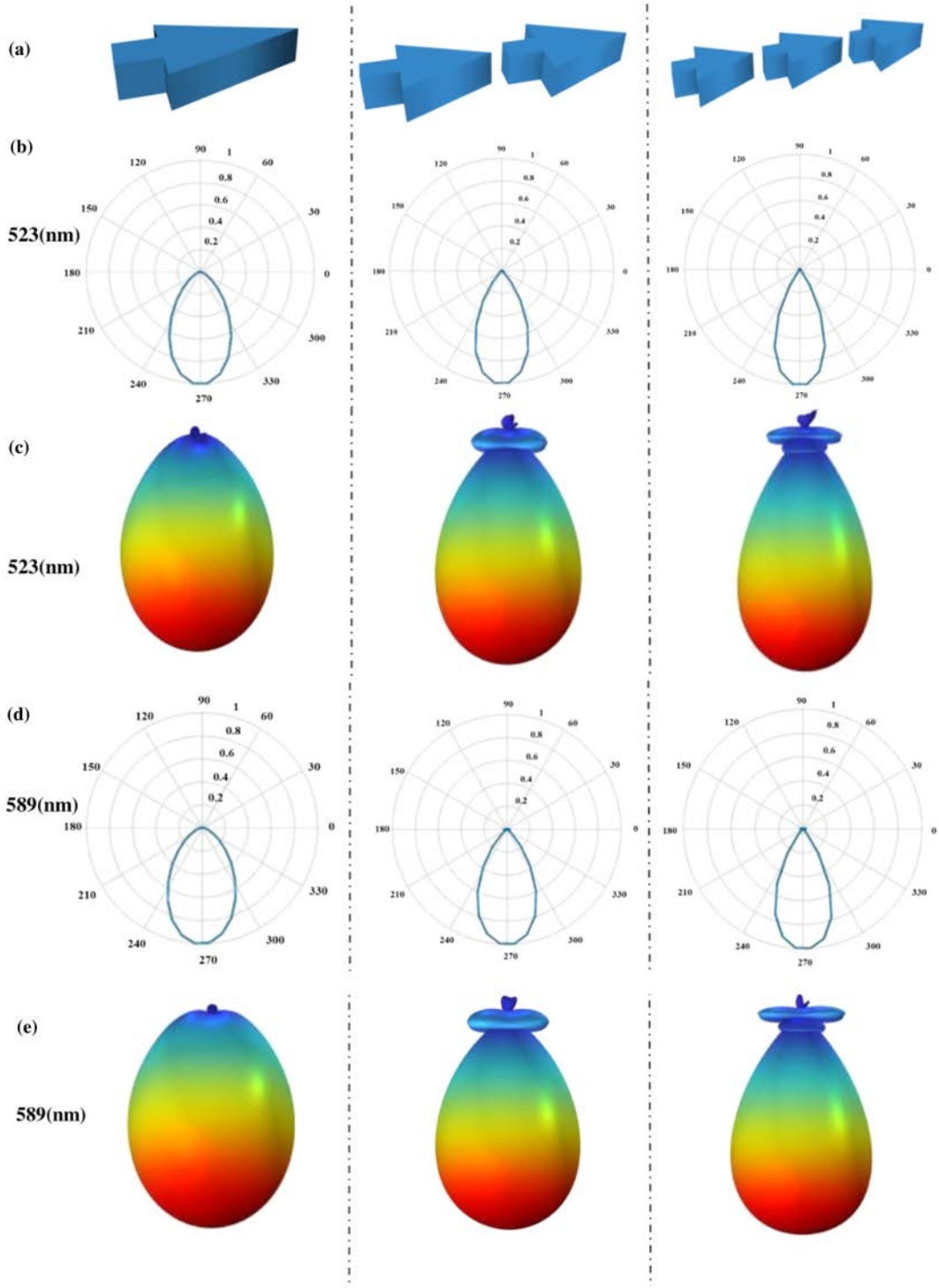

Fig. 8. (a) Arrays of dielectric nanoantennas with the interparticle distance L. (b) 2D and (c) 3D radiated patterns of the antenna for $N = 1, 2, 3$ at $\lambda = 523$ nm. (d) 2D and (e) 3D radiated patterns of the antenna for $N = 1, 2, 3$ at $\lambda = 589$ nm.

The magnitude of the Purcell factor is a valuable parameter to measure the electric dipole emission of the nanoantenna. Here, six points, A, B, C, D, E, and F, are chosen in the direction of the positive half-axis of the y-axis and the xz-plane as marked in Fig. 9(a). By keeping the polarization of the incident light along the x-axis and the propagation direction along the $+z$-axis constant, the electric dipole source is placed at the six points, and the properties of the ED emitter are determined by calculating the Purcell factor (PF), as shown in Fig. 9(b).The electric dipole source at point A has the largest Purcell coefficient of about 4.5×10^9, followed by points C and F. The PFs of the other three points are nearly zero. Similarly, a magnetic dipole source is placed at these six points to study the MD emitter. As shown in Fig. 9(c), the magnetic dipole source shows the maximum

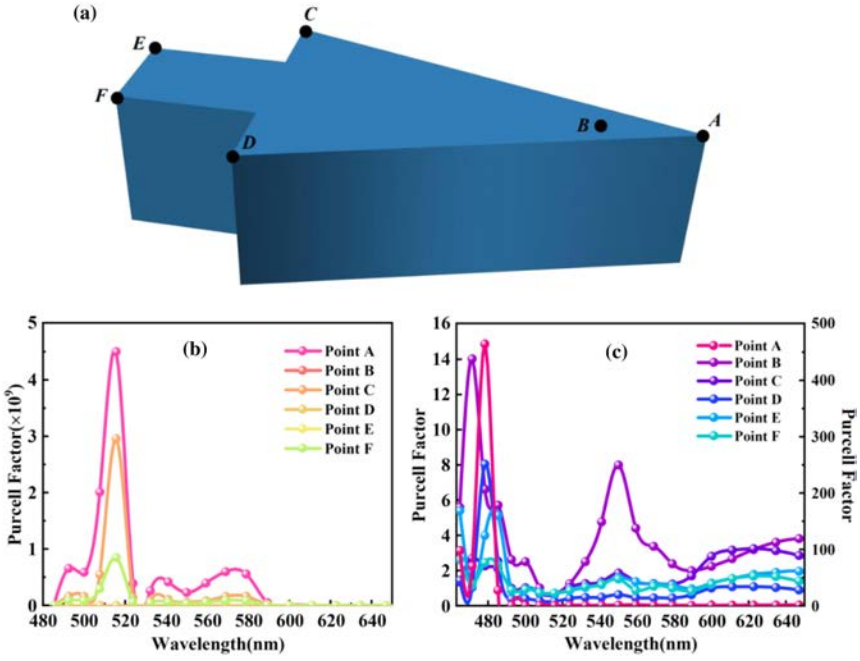

Fig. 9. (a) Locations of the six points in the nanostructure (marked as A, B, C, D, E, and F) selected for the study of the Purcell factor and (b) the electric dipole excitation and (c) the magnetic dipole excitation.

Table 1. Comparison of the Characteristics of Our Nanoantenna with Those of Recently Reported Nanoantennas (Purcell Factor)

References	Characteristics	Purcell Factor	Structure
[47]	Hexagonal InP nanowire	4.72	
[48]	Silicon cuboid nanoantenna	18115	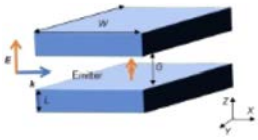
[49]	Erbium ions in TiO_2 on silicon nanocavities	200	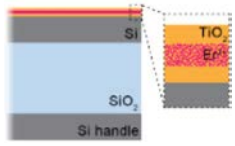
[50]	HMM + PNCs and HMM + PNCs + nanoantenna	2.8–3.9	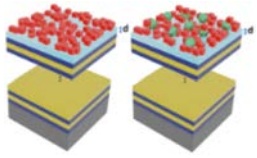
[51]	Nanopillar antenna-resonator in 4H-SiC and Ag	120.6	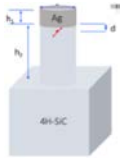
This work	Gallium phosphide arrow-shaped nanoantenna	4.5×10^9	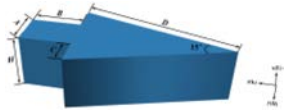

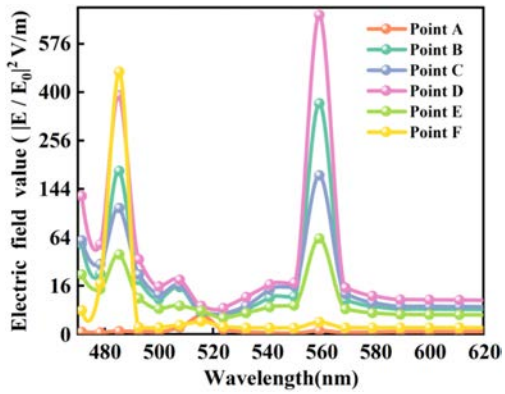

Fig. 10. Electric fields at the selected points of A, B, C, D, E, and F.

value at point A with a value of 464.68. The PFs of the magnetic dipole sources at points B, D, E, and F show significant numerical fluctuations in the 460–650 nm wavelength range. There are four clear peaks at point B, the two most pronounced ones with PFs of 14.02 at 471 nm and 7.99 at 550 nm. In summary, the emissions of both the electric and magnetic dipole sources in the arrow-type nanostructures increase significantly, confirming that the nanoantenna has large potential in applications such as quantum transmitters and fluorescence enhancement.

In recent years, various nanoantennas with unidirectional scattering functions have been proposed, but how to simultaneously improve the performance of spontaneous radiation remains a difficult challenge. In this regard, our nanostructure has superior radiation properties, as shown in Table 1.

In addition to the investigation of the far-field characteristics, the electric field enhancement in the near field is analyzed. Here, six points are selected to verify whether the electric field enhancement can be achieved by calculating the electric fields. The color lines in Fig. 10 display the electric fields at these six points. The curves show that the electric field at point F is the largest when the wavelength is 485 nm reaching 470.46, while the electric field of 696.33 at point D is the largest at 559 nm. The data show that the enhanced coupling of photons and electrons increases the near-field potential and near-field intensity, boding well for surface enhancement and surface-enhanced Raman scattering (SERS).

Finally, since the influence of the surface plays a prominent role in the performance of nanoantennas, we investigated a novel metasurface composed of arrow-shaped nanoantennas [52] and metasurfaces [53]. Figure 11(a) schematically illustrates the metasurface of the same arrow-shaped nanoantenna illuminated by a perpendicular incident wave. In order to gain a deeper understanding of its characteristics, the scattering power of different multipoles in the Cartesian coordinate system was calculated, including the electric dipole (ED), the magnetic dipole (MD), the toroidal dipole (TD), the electric quadrupole (EQ), and the magnetic quadrupole (MQ), and plotted in Fig. 11(b). It can be clearly observed that the contribution of the TD is dominant, followed by the EQ playing a certain role. In addition, the transmittance was computed in accordance with the left y-axis and reached a maximum value of 0.85 at 374 nm, indicating its periodic dependence on ultra-high transmission performance.

4. CONCLUSION

A nanoantenna (arrow-type nanoantenna) composed of the high-refractive-index dielectric gap materials exhibits highly unidirectional forward scattering in the visible range. The antenna shows not only far-field unidirectional scattering, but also high forwardness at multiple operating wavelengths. Parameters such as the thickness and arrow angle are very sensitive to the intensity of unidirectional scattering. Therefore, unidirectional scattering can be tuned by changing the structural parameters. Increasing the number of nanoparticles in the array can further enhance forward scattering. The electric field intensity and Purcell factors under excitation by electric and magnetic dipole sources are calculated. The electric field enhancement is 700, which is much higher than that of the silicon nanodisk. The remarkable field enhancement and multiple unidirectional responses are crucial factors for nanoresonators. Our study on unidirectional scattering provides a feasible solution for designing and modulating the optical properties

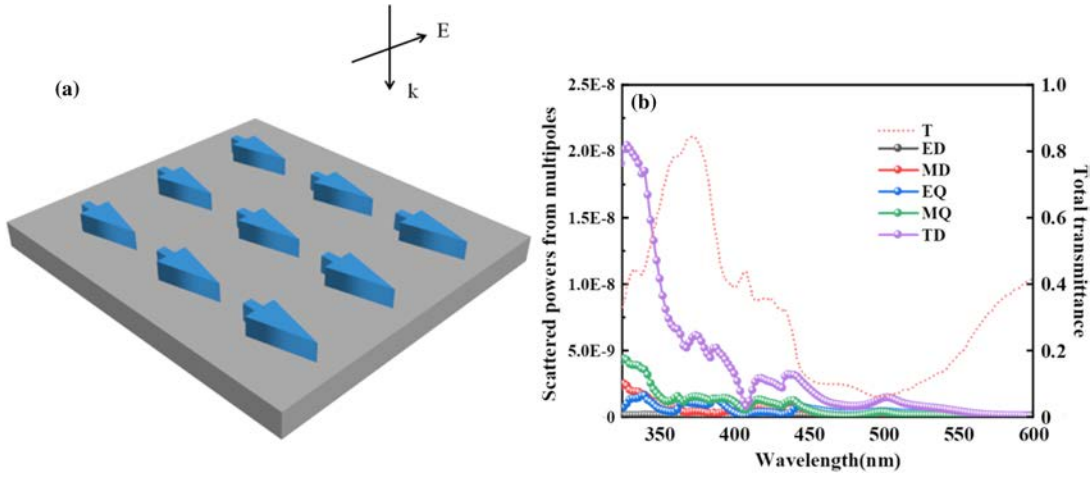

Fig. 11. (a) Schematic of a novel metasurface consisting of an arrow-shaped nanoantenna, where the substrate is SiO_2 with $n = 1.44$ and the incident light is irradiated vertically and (b) scattered powers from multipoles and the total transmittance.

of nanoantennas, thus providing novel nanoantennas for applications such as biosensors and photovoltaic devices.

Funding. Natural Science Foundation of Heilongjiang Province (LH2023F007); Outstanding Young and Middle-Aged Research and Innovation Team of Northeast Petroleum University (KYCXTD201801); Research Initiation Project of Northeast Petroleum University (2019KQ74); Study Abroad returnees merit based Aid Foundation in Heilongjiang Province (070-719900103); City University of Hong Kong Donation Research Grant (9229021); City University of Hong Kong Strategic Research Grant (SRG) (7005505); China Postdoctoral Science Foundation funded project (2020M670881); Local Universities Reformation and Development Personnel Training Supporting Project from Central Authorities.

Disclosures. The authors declare no conflicts of interest.

Data availability. Data underlying the results presented in this paper are not publicly available at this time but may be obtained from the authors upon reasonable request.

Supplemental document. See Supplement 1 for supporting content.

REFERENCES

1. J.-N. Wang, B. Xiong, Y. Liu, C.-W. Chen, D.-X. Qi, B.-Q. Hou, R. Peng, and M. Wang, "Continuously and reversibly electro-tunable optical nanoantennas based on phase transition of vanadium dioxide," New J. Phys. **23**, 075002 (2021).
2. A. J. Wilson and P. K. Jain, "Light-induced voltages in catalysis by plasmonic nanostructures," Acc. Chem. Res. **53**, 1773–1781 (2020).
3. H. Ren, X. Ren, K. Niu, S. Wang, Z. Huang, and X. Wu, "Optical-electrical-thermal optimization of plasmon-enhanced perovskite solar cells," Phys. Chem. Chem. Phys. **22**, 17068–17074 (2020).
4. M. M. Salary, S. Jafar-Zanjani, and H. Mosallaei, "Nonreciprocal optical links based on time-modulated nanoantenna arrays: full-duplex communication," Phys. Rev. B **99**, 045416 (2019).
5. W. Liu, C. Hu, L. Zhou, Z. Yi, C. Liu, J. Lv, L. Yang, and P. K. Chu, "A square-lattice D-shaped photonic crystal fiber sensor based on SPR to detect analytes with large refractive indexes," Physica E **138**, 115106 (2022).
6. C. Liu, J. Lv, W. Liu, F. Wang, and P. K. Chu, "Overview of refractive index sensors comprising photonic crystal fibers based on the surface plasmon resonance effect [Invited]," Chin. Opt. Lett. **19**, 102202 (2021).
7. L. Xin, M. Lu, S. Both, M. Pfeiffer, M. J. Urban, C. Zhou, H. Yan, T. Weiss, N. Liu, and K. Lindfors, "Watching a single fluorophore molecule walk into a plasmonic hotspot," ACS Photonics **6**, 985–993 (2019).
8. S. Arslanagić and R. W. Ziolkowski, "Cylindrical and spherical active coated nanoparticles as nanoantennas: active nanoparticles as nanoantennas," IEEE Antennas Propag. Mag. **59**, 14–29 (2017).
9. H. Ago, S. Okada, Y. Miyata, K. Matsuda, M. Koshino, K. Ueno, and K. Nagashio, "Science of 2.5 dimensional materials: paradigm shift of materials science toward future social innovation," Sci. Technol. Adv. Mater. **23**, 275–299 (2022).
10. J. Cambiasso, G. Grinblat, Y. Li, A. Rakovich, E. Cortés, and S. A. Maier, "Bridging the gap between dielectric nanophotonics and the visible regime with effectively lossless gallium phosphide antennas," Nano Lett. **17**, 1219–1225 (2017).
11. L. Hüttenhofer, A. Tittl, L. Kühner, E. Cortés, and S. A. Maier, "Anapole-assisted absorption engineering in arrays of coupled amorphous gallium phosphide nanodisks," ACS Photonics **8**, 1469–1476 (2021).
12. D. Shima, H. Sugimoto, A. Assadillayev, S. Raza, and M. Fujii, "Gallium phosphide nanoparticles for low-loss nanoantennas in visible range," Adv. Opt. Mater. **11**, 2203107 (2023).
13. X. M. Zhang, Q. Zhang, S. J. Zeng, Z. Z. Liu, and J.-J. Xiao, "Dual-band unidirectional forward scattering with all-dielectric hollow nanodisk in the visible," Opt. Lett. **43**, 1275–1278 (2018).
14. Y. H. Fu, A. I. Kuznetsov, A. E. Miroshnichenko, Y. F. Yu, and B. Luk'yanchuk, "Directional visible light scattering by silicon nanoparticles," Nat. Commun. **4**, 1527 (2013).
15. H. S. Ee, J. H. Kang, M. L. Brongersma, and M. K. Seo, "Shape-dependent light scattering properties of subwavelength silicon nanoblocks," Nano Lett. **15**, 1759–1765 (2015).
16. B. Rolly, B. Stout, and N. Bonod, "Boosting the directivity of optical antennas with magnetic and electric dipolar resonant particles," Opt. Express **20**, 20376–20386 (2012).
17. M. R. Hasan and O. G. Hellesø, "Dielectric optical nanoantennas," Nanotechnology **32**, 202001 (2021).
18. H. Zhang, J. Cadusch, C. Kinnear, T. James, A. Roberts, and P. Mulvaney, "Direct assembly of large area nanoparticle arrays," ACS Nano **12**, 7529–7537 (2018).
19. I. M. Hancu, A. G. Curto, M. Castro-López, M. Kuttge, and N. F. Hulst, "Multipolar interference for directed light emission," Nano Lett. **14**, 166–171 (2014).
20. X. Zhang, Q. Zhang, Y. Yuan, J. Liu, and X. Liu, "Ultra-directional forward scattering by a high refractive index dielectric T-shaped nanoantenna in the visible," Phys. Lett. A **384**, 126696 (2020).
21. Y. Yu, J. Liu, Y. Yu, D. Qiao, Y. Li, and R. Salas-Montiel, "Broadband unidirectional transverse light scattering in a V-shaped silicon nanoantenna," Opt. Express **30**, 7918–7927 (2022).
22. P. D. Terekhov, K. V. Baryshnikova, A. S. Shalin, A. Karabchevsky, and A. B. Evlyukhin, "Resonant forward scattering of light by high-refractive-index dielectric nanoparticles with toroidal dipole contribution," Opt. Lett. **42**, 835–838 (2017).
23. P. D. Terekhov, A. B. Evlyukhin, A. S. Shalin, and A. Karabchevsky, "Polarization-dependent asymmetric light scattering by silicon nanopyramids and their multipoles resonances," J. Appl. Phys. **125**, 173108 (2019).
24. L. Novotny and N. van Hulst, "Antennas for light," Nat. Photonics **5**, 83–90 (2011).
25. A. G. Curto, G. Volpe, T. H. Taminiau, M. P. Kreuzer, R. Quidant, and N. F. van Hulst, "Unidirectional emission of a quantum dot coupled to a nanoantenna," Science **329**, 930–933 (2010).
26. H. A. Atwater and A. Polman, "Plasmonics for improved photovoltaic devices," Nat. Mater. **9**, 205–213 (2010).
27. Z. Yi, L. Liu, L. Wang, C. Cen, X. Chen, Z. Zhou, X. Ye, Y. Yi, Y. Tang, Y. Yi, and P. Wu, "Tunable dual-band perfect absorber consisting of periodic cross-cross monolayer graphene arrays," Results Phys. **13**, 102217 (2019).
28. R. de la Rica and M. M. Stevens, "Plasmonic ELISA for the ultrasensitive detection of disease biomarkers with the naked eye," Nat. Nanotechnol. **7**, 821–824 (2012).
29. P. L. Stiles, J. A. Dieringer, N. C. Shah, and R. P. Van Duyne, "Surface-enhanced Raman spectroscopy," Annu. Rev. Anal. Chem. **1**, 601–626 (2008).
30. H. A. Abudayyeh and R. Rapaport, "Quantum emitters coupled to circular nanoantennas for high-brightness quantum light sources," Quantum Sci. Technol. **2**, 034004 (2017).
31. A. B. Evlyukhin, T. Fischer, C. Reinhardt, and B. N. Chichkov, "Optical theorem and multipole scattering of light by arbitrarily shaped nanoparticles," Phys. Rev. B **94**, 205434 (2016).
32. C. Xu, K. Cheng, Q. Li, X. Shang, C. Wu, Z. Wei, X. Zhang, and H. Li, "The dual-frequency zero-backward scattering realized in a hybrid metallo-dielectric nanoantenna," AIP Adv. **9**, 075121 (2019).
33. W. Liu, Y. Shi, Z. Yi, C. Liu, F. Wang, X. Li, J. Lv, L. Yang, and P. K. Chu, "Surface plasmon resonance chemical sensor composed of a microstructured optical fiber for the detection of an ultra-wide refractive index range and gas-liquid pollutants," Opt. Express. **29**, 40734–40747 (2021).
34. W. Liu, C. Liu, J. Wang, J. Lv, Y. Lv, L. Yang, N. An, Z. Yi, Q. Liu, C. Hu, and P. K. Chu, "Surface plasmon resonance sensor composed of microstructured optical fibers for monitoring of external and internal environments in biological and environmental sensing," Results Phys. **47**, 106365 (2023).
35. V. Remesh, G. Grinblat, Y. Li, S. A. Maier, and N. F. Hulst, "Coherent multiphoton control of gallium phosphide nanodisk resonances," ACS Photonics **6**, 2487–2491 (2019).

36. J. Lv, D. Wang, C. Liu, J. Wang, L. Yang, W. Liu, Q. Liu, H. Mu, and P. K. Chu, "Theoretical analysis of hybrid metal–dielectric nanoantennas with plasmonic Fano resonance for optical sensing," Coatings **12**, 1248 (2022).
37. E. D. Palik, *Handbook of Optical Constants of Solids* (Academic, 1985).
38. D. K. Oh, Y. Kim, J. Kim, I. Kim, and J. Rho, "Guided domino lithography for uniform fabrication of single-digit-nanometer scale plasmonic nanoantenna," Nanophotonics **12**, 1435–1441 (2023).
39. P. D. Terekhov, K. V. Baryshnikova, Y. A. Artemyev, A. Karabchevsky, A. S. Shalin, and A. B. Evlyukhin, "Multipolar response of nonspherical silicon nanoparticles in the visible and near-infrared spectral ranges," Phys. Rev. B **96**, 035443 (2017).
40. J. Lv, H. Zhang, C. Liu, Z. Yi, F. Wang, H. Mu, X. Li, T. Sun, and P. K. Chu, "Optical anapole modes in gallium phosphide nanodisk with forked slits for electric field enhancement," Nanomaterials **11**, 1490 (2021).
41. N. Li, Y. Lai, S. H. Lam, H. Bai, L. Shao, and J. Wang, "Directional control of light with nanoantennas," Adv. Opt. Mater. **9**, 2001081 (2021).
42. P. D. Terekhov, H. K. Shamkhi, E. A. Gurvitz, K. V. Baryshnikova, A. B. Evlyukhin, A. S. Shalin, and A. Karabchevsky, "Broadband forward scattering from dielectric cubic nanoantenna in lossless media," Opt. Express **27**, 10924–10935 (2019).
43. A. K. M. Naziul Haque, T. Ahmed, and M. Z. Baten, "In-plane directionality control of strongly localized resonant modes of light in disordered arrays of dielectric scatterers," Opt. Express **29**, 39227–39240 (2021).
44. A. E. Krasnok, A. P. Slobozhanyuk, C. R. Simovski, S. A. Tretyakov, A. N. Poddubny, A. E. Miroshnichenko, Y. S. Kivshar, and P. A. Belov, "An antenna model for the Purcell effect," Sci. Rep. **5**, 12956 (2015).
45. F. Lou, M. Yan, L. Thylen, M. Qiu, and L. Wosinski, "Whispering gallery mode nanodisk resonator based on layered metal-dielectric waveguide," Opt. Express **22**, 8490 (2014).
46. A. N. Poddubny, P. A. Belov, and Y. S. Kivshar, "Spontaneous radiation of a finite-size dipole emitter in hyperbolic media," Phys. Rev. A **84**, 23807 (2011).
47. S. Mohammadnejad, A. A. Mahmoudi, and H. Arab, "A new III–V nanowire-quantum dot single photon source with improved Purcell factor for quantum communication," Opt. Quantum Electron. **54**, 220 (2021).
48. Q. Deng, J. Chen, L. Long, B. Chen, H. Yu, and Z. Li, "Silicon cuboid nanoantenna with simultaneous large Purcell factor for electric dipole, magnetic dipole and electric quadrupole emission," Opto-Electron. Adv. **5**, 210024 (2022).
49. A. M. Dibos, M. T. Solomon, S. E. Sullivan, M. K. Singh, K. E. Sautter, C. P. Horn, G. D. Grant, Y. Lin, J. Wen, F. J. Heremans, S. Guha, and D. D. Awschalom, "Purcell enhancement of erbium ions in TiO_2 on silicon nanocavities," Nano Lett. **22**, 6530–6536 (2022).
50. H. P. Adl, S. Gorji, M. K. Habil, I. Suárez, V. S. Chirvony, A. F. Gualdrón-Reyes, I. Mora-Seró, L. M. Valencia, M. de la Mata, J. Hernández-Saz, S. I. Molina, C. J. Zapata-Rodríguez, and J. P. Martínez-Pastor, "Purcell enhancement of the spontaneous emission of $CsPbI_3$ perovskite nano-crystals coupled to hyperbolic metamaterials," ACS Photonics **7**, 3152–3160 (2020).
51. F. A. Inam and S. Castelletto, "Metal-dielectric nanopillar antenna-resonators for efficient collected photon rate from silicon carbide color centers," Nanomaterials **13**, 195 (2023).
52. A. V. Prokhorov, P. D. Terekhov, M. Y. Gubin, A. V. Shesterikov, X. Ni, V. R. Tuz, and A. B. Evlyukhin, "Resonant light trapping via lattice-induced multipole coupling in symmetrical metasurfaces," ACS Photonics **9**, 3869–3875 (2022).
53. H. K. Shamkhi, K. V. Baryshnikova, A. Sayanskiy, P. Kapitanova, P. D. Terekhov, P. Belov, A. Karabchevsky, A. B. Evlyukhin, Y. Kivhar, and A. S. Shalin, "Transverse scattering and generalized Kerker effects in all-dielectric Mie-resonant metaoptics," Phys. Rev. Lett. **122**, 19305 (2019).

Supplemental Document

Journal of the Optical Society of America A
OPTICS, IMAGE SCIENCE, AND VISION

Multi-wavelength unidirectional forward scattering properties of the arrow-shaped gallium phosphide nanoantenna: supplement

JINGWEI LV,[1] YANRU REN,[1] DEBAO WANG,[1] XINCHEN XU,[1] WEI LIU,[1] JIANXIN WANG,[1] CHAO LIU,[1,*] AND PAUL K CHU[2]

[1]*School of Physics and Electronic Engineering, Northeast Petroleum University, Daqing 163318, China*
[2]*Department of Physics, Department of Materials Science and Engineering, and Department of Biomedical Engineering,City University of Hong Kong, Tat Chee Avenue, Kowloon, Hong Kong, China*
[*]*msm-liu@126.com*

Supplement DOI: https://doi.org/10.6084/m9.figshare.24231568

Parent Article DOI: https://doi.org/10.1364/JOSAA.496501

During fabrication, the arrow-shaped antenna is likely to be diluted/eroded due to the sharp angle, so we chipped off a piece of the arrow-shaped nanoantenna tip structure and calculated its unidirectional scattering properties. Based on the original structure of the arrow-shaped nanoantenna, the tip part is chipped off in Fig. S1(a). Fig. S1(b) shows the angular distribution of the two-dimensional (2D) far-field scattering intensities at the wavelengths of 507 nm, 523 nm, and 589 nm. The significant suppression of BS and a strong enhancement of FS can still be observed, and unidirectional scattering is still achievable. Further, the corresponding three-dimensional (3D) far-field patterns are presented in Fig. S1(c). In summary, it can be seen that the arrow-shaped nanoantenna with the tip cut off can still exhibit unidirectional scattering.

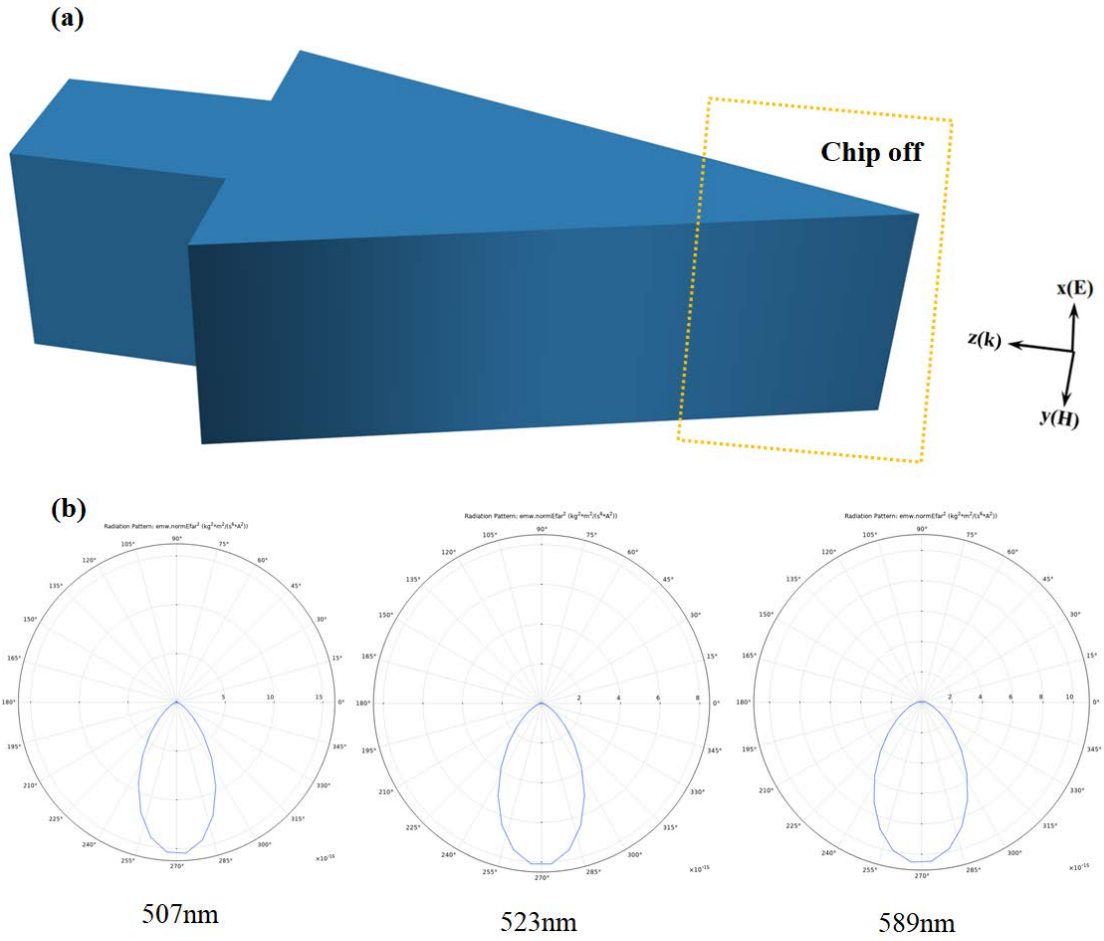

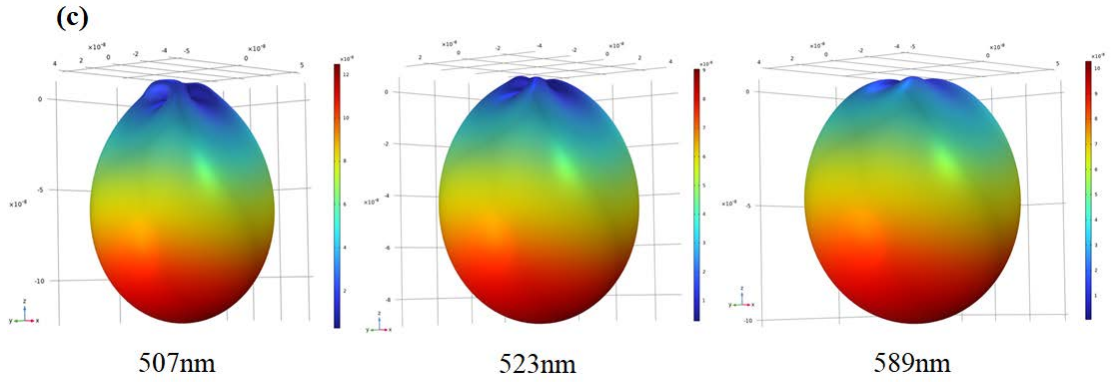

Fig.S1.(a) Structural diagram and(b)scattering patterns of the nanoantenna (2D) and (c) 3D far-field radiation patterns of the nanoantenna.